iScience

CellPress
OPEN ACCESS

Article

Chemogenetic activation of nigrostriatal dopamine neurons in freely moving common marmosets

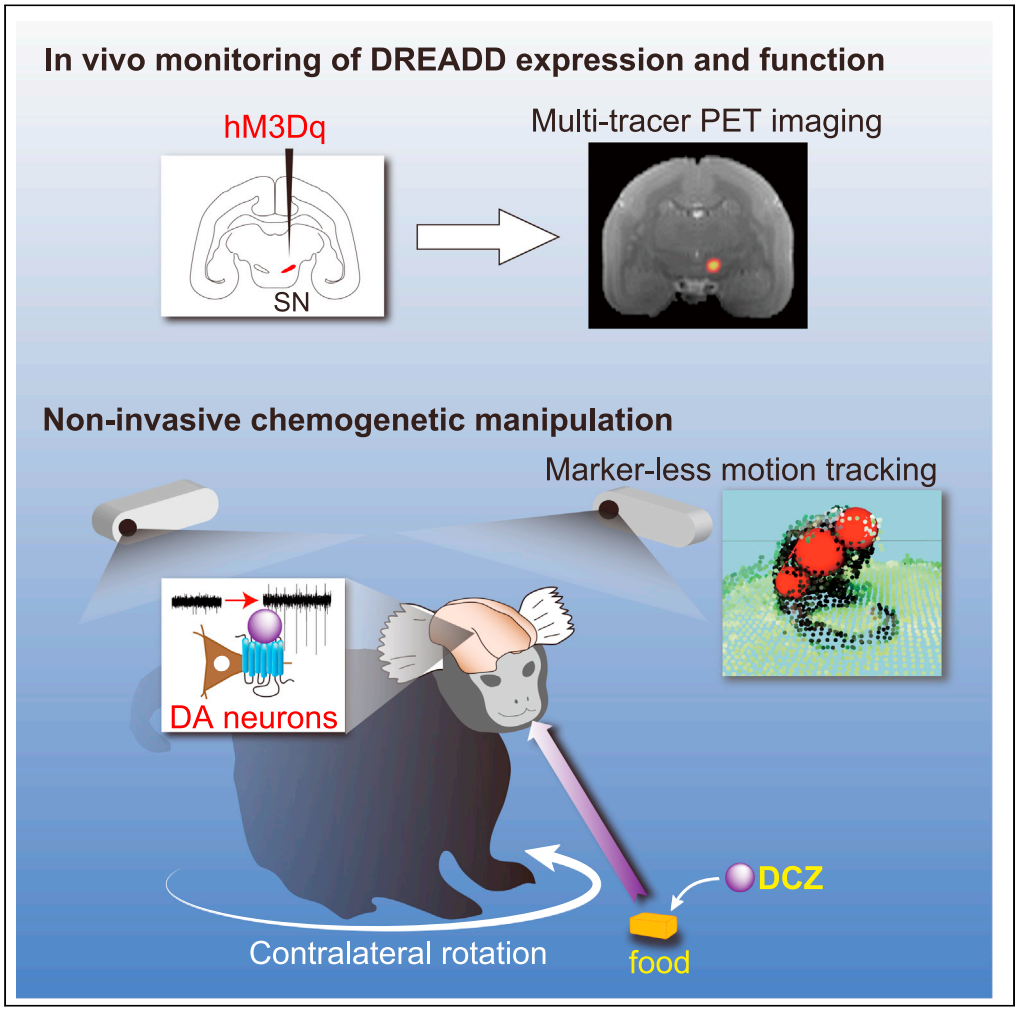

Koki Mimura, Yuji Nagai, Ken-ichi Inoue, ..., Tetsuya Suhara, Makoto Higuchi, Takafumi Minamimoto

minamimoto.takafumi@qst.go.jp

Highlights

DREADDs were applied to activate unilateral nigrostriatal dopamine neurons

DREADD expression/function and marmoset behavior were monitored non-invasively

Orally delivered DREADD actuator reversibly induced contralateral rotation behavior

Non-invasive chemogenetic manipulation will broaden the utility of marmosets

Mimura et al., iScience 24, 103066
September 24, 2021
https://doi.org/10.1016/j.isci.2021.103066

iScience

CellPress
OPEN ACCESS

Article

Chemogenetic activation of nigrostriatal dopamine neurons in freely moving common marmosets

Koki Mimura,[1] Yuji Nagai,[1] Ken-ichi Inoue,[2] Jumpei Matsumoto,[3,4] Yukiko Hori,[1] Chika Sato,[5,6] Kei Kimura,[2] Takashi Okauchi,[1] Toshiyuki Hirabayashi,[1] Hisao Nishijo,[3,4] Noriaki Yahata,[5,6] Masahiko Takada,[2] Tetsuya Suhara,[1] Makoto Higuchi,[1] and Takafumi Minamimoto[1,7,*]

SUMMARY

To interrogate particular neuronal pathways in nonhuman primates under natural and stress-free conditions, we applied designer receptors exclusively activated by designer drugs (DREADDs) technology to common marmosets. We injected adeno-associated virus vectors expressing the excitatory DREADD hM3Dq into the unilateral substantia nigra (SN) in four marmosets. Using multi-tracer positron emission tomography imaging, we detected DREADD expression in vivo, which was confirmed in nigrostriatal dopamine neurons by immunohistochemistry, as well as by assessed activation of the SN following agonist administration. The marmosets rotated in a contralateral direction relative to the activated side 30–90 min after consuming food containing the highly potent DREADD agonist deschloroclozapine (DCZ) but not on the following days without DCZ. These results indicate that non-invasive and reversible DREADD manipulation will extend the utility of marmosets as a primate model for linking neuronal activity and natural behavior in various contexts.

INTRODUCTION

There has been growing interest in the common marmoset (*Callithrix jacchus*), a small nonhuman primate, as a neurobiological model of the human brain in both health and disease (Mitchell and Leopold, 2015; Miller et al., 2016; Ausderau et al., 2017). Owing to their rich natural behavioral repertoires with learning capabilities, marmosets have been used in a number of studies to examine the neural basis of cognitive, emotional, and social functions (Suzuki et al., 2015; Takahashi et al., 2017; Koshiba et al., 2011). For example, a variety of functions of the nigrostriatal dopamine (DA) system have been studied in freely behaving marmosets, including cognitive flexibility (Clarke et al., 2011), discrimination learning (Takaji et al., 2016), and motor activity (Ando et al., 2012), through irreversible manipulation of the DA system such as DA depletion and receptor knockdown. However, given that individual variability is less controllable in behavioral examinations, especially under freely moving conditions, reversible manipulation is more advantageous because it permits within-subject comparisons. Reversible manipulation is possible via local drug infusion (Horst et al., 2019); however, this requires that subjects are captured and held for every manipulation, thereby causing potential adverse reactions (e.g., stress) that could confound the main effects. As such, the conventional manipulation methodologies have some limitations for the reversible and stress-free interrogation of particular neural systems, preventing neuroscientists from taking advantage of the rich natural behavior of marmosets and extending their utility as a primate model.

Chemogenetic technology designer receptors exclusively activated by designer drugs (DREADDs) afford a minimally invasive means of reversibly and remotely controlling the activity of a neuronal population expressing designer receptors through systemic delivery of their agonist (Alexander et al., 2009; Roth, 2017). DREADDs have widely been used to modify neuronal activity and behavior in rodents. They have also proven valuable in nonhuman primates, allowing reversible manipulation of activity across a specific neuronal population in large and discontinuous brain regions that are beyond the reach of pharmacological, electrical, or optogenetic manipulation strategies (Eldridge et al., 2016; Upright et al., 2018; Nagai et al., 2016, 2020). Because there is no requirement for chronic surgical implantation of any invasive devices, DREADDs permit flexible experimental designs to control neuronal activity in freely moving marmosets

[1]Department of Functional Brain Imaging, National Institutes for Quantum and Radiological Science and Technology, Chiba 263-8555 Japan

[2]Systems Neuroscience Section, Primate Research Institute, Kyoto University, Inuyama, Aichi 484-8506, Japan

[3]Department of System Emotional Science, Faculty of Medicine, University of Toyama, Toyama 930-8555, Japan

[4]Research Center for Idling Brain Science, University of Toyama, Toyama 930-8555, Japan

[5]Quantum Life Informatics Group, Institute for Quantum Life Science, National Institutes for Quantum and Radiological Science and Technology, Chiba 263-8555 Japan

[6]Applied MRI Research, Department of Molecular Imaging and Theranostics, National Institutes for Quantum and Radiological Science and Technology, Chiba 263-8555 Japan

[7]Lead contact

*Correspondence: minamimoto.takafumi@qst.go.jp

https://doi.org/10.1016/j.isci.2021.103066

Table 1. Summary of subject information and experiments

ID	Sex	Target	Vector	MRI	[^{11}C]DCZ	[^{18}F]FDG	Behavior	Histology
Marmo1	Male	Left SN	AAV2.1-hSyn1-hM3Dq-IRES-AcGFP	+	+		+	+
Marmo2	Male	Right SN	AAV2.1-hSyn1-hM3Dq-IRES-AcGFP	+	+		+	+
Marmo3	Female	Left SN	AAV2-CMV-hM3Dq, AAV2-CMV-AcGFP	+	+	+		+
Marmo4	Female	Left SN	AAV2.1-TH-FLAG-hM3Dq	+	+	+	+	+

SN, substantia nigra; MRI, magnetic resonance imaging; [^{11}C]DCZ, [^{11}C]deschloroclozapine; [^{18}F]FDG, [^{18}F]fluorodeoxyglucose; AcGFP, Aequorea coerulescens green fluorescent protein.

with minimal invasiveness. To date, no study has reported the application of DREADD-based neuronal control in behaving marmosets.

To apply DREADDs technology to marmosets, strategies used for macaque monkeys, such as viral vector delivery and non-invasive monitoring of DREADD expression and function, should be useful and applicable. In addition, the use of the highly potent novel DREADD agonist deschloroclozapine (DCZ) should provide a wider effective window for the selective activation of DREADDs with minimal off-target effects, as demonstrated in mice and macaques (Nagai et al., 2020). However, conventional routes of agonist administration, such as intramuscular and intraperitoneal (IP) injections, can induce pain and stress, leading to unwanted effects on natural behavior. Because DCZ displays good brain penetrability and metabolic stability in macaques, oral delivery (per os [PO]) is a feasible alternative route for non-invasive DCZ administration for marmosets.

We performed a proof-of-concept study employing non-invasive chemogenetic manipulation of a specific neural system in freely moving marmosets. We aimed to increase the excitability of nigrostriatal DA neurons, which is known to induce rotational behavior in rodents (Smith et al., 1996; van der Heyden, 1984; Arbuthnott and Ungerstedt, 1975). Marmosets received injections of adeno-associated virus (AAV) vectors expressing the excitatory DREADD hM3Dq into unilateral substantia nigra (SN). Subsequent multimodal positron emission tomography (PET) imaging was used to assess the DREADD expression and function following agonist administration. We revealed that oral DCZ administration reversibly induced contralateral rotation behavior. Our results demonstrated that non-invasive chemogenetic manipulation can enhance the utility of marmosets as a primate model for linking a particular neural pathway and non-restricted behavior in a variety of contexts.

RESULTS

Imaging-guided transduction and monitoring hM3Dq expression in unilateral SN

Four marmosets received an injection of AAV vectors co-expressing hM3Dq with a fluorescent marker (green fluorescent protein; GFP) or a fusion protein (FLAG tag) into one side of the SN under intraoperative X-ray computed tomography (CT) guidance (Table 1; Figures 1A and 1B). Another control vector expressing a fluorescent protein marker [monomeric Kusabira Orange (mKO) or GFP] was also injected into the opposite side. More than 6 weeks after the injection, we performed PET using the DREADD-selective radioligand [^{11}C]DCZ to visualize hM3Dq expression in vivo, as demonstrated previously in macaque monkeys (Nagai et al., 2020). hM3Dq expression in the SN was visualized as a region exhibiting high radioligand binding (Figure 1C). The binding potential relative to a non-displaceable binding (BP_{ND}) of [^{11}C]DCZ in the target SN was significantly higher than that of the contralateral side ($p = 0.04$, t value = 3.45, paired t test; N = 4; Figure 1D). Postmortem immunohistochemical analysis confirmed that GFP, a marker of transgene expression, was expressed in the neurons on the target side of the SN pars compacta (SNc) in all subjects (e.g., Figures 1E and 1F). A confocal micrograph shows that there are many double-labeled cells expressing hM3Dq (reported by GFP) and DA cell marker (tyrosine hydroxylase, TH) (Figure 1G, white arrowheads). GFP expression was also found in the ipsilateral striatum, the area receiving direct projections from the SNc (Figures 1H–1K). Thus, these results suggested that hM3Dq was introduced in the dopaminergic neurons in the SNc unilaterally in all four subjects.

Chemogenetic activation of unilateral nigrostriatal DA neurons

Next, we tried to induce and monitor chemogenetic activation of unilateral nigrostriatal neurons by hM3Dq. In this experiment, we used clozapine N-oxide (CNO) and the highly potent and selective DREADD

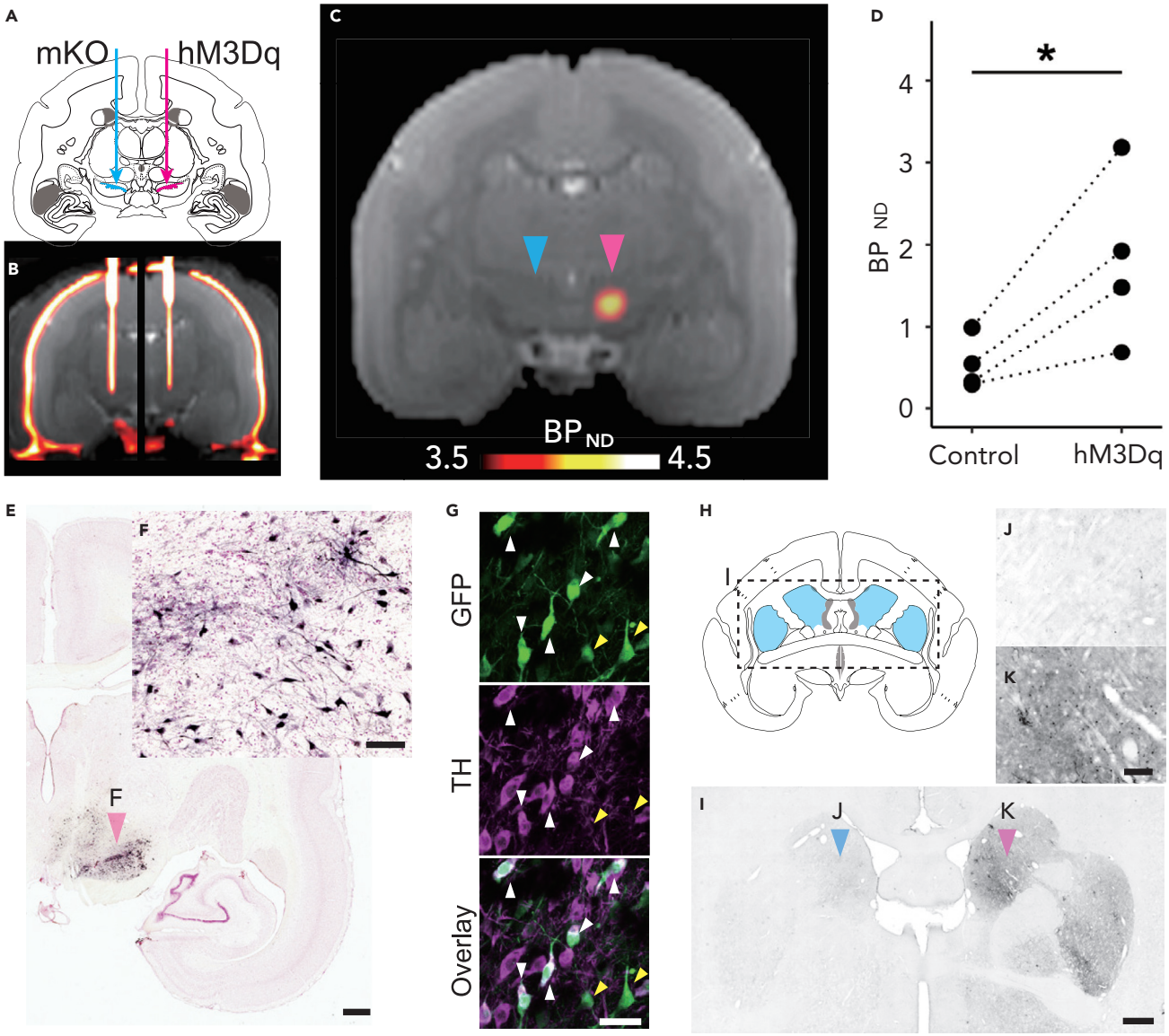

Figure 1. Imaging-guided injection of adeno-associated virus (AAV) vectors and evaluation of hM3Dq expression

(A) Illustration of the location of viral vector injections. AAV vectors expressing hM3Dq were injected into the unilateral substantia nigra (SN, red arrow). As control, an AAV vector expressing a fluorescent marker was injected into the contralateral SN (blue arrow).

(B) A coronal computed tomography image overlaid on a magnetic resonance image representing the position of the vector injection needle obtained during surgery.

(C) A coronal representative parametric positron emission tomography image showing the specific binding (BP_{ND}) of [^{11}C]deschloroclozapine (DCZ; Day 43, Marmo1). Red and blue arrowheads denote hM3Dq- and mKO-expressing sides, respectively.

(D) Comparison of regional BP_{ND} of [^{11}C]DCZ between the hM3Dq and control side of the SN for three marmosets, where dotted lines connect individual data. The asterisk indicates a significant difference ($p < 0.05$, pairwise t test).

(E) A photograph of the representative coronal section staining for green fluorescent protein (GFP) and neutral red including the SN (Marmo1). Scale bar = 1 mm.

(F) A high-magnification image of SN neurons (red arrowhead in E). Scale bar = 100 μm.

(G) Confocal images of co-staining of GFP and TH in SNc region (Marmo2). Scale bar = 50 μm. White and yellow arrowheads represent double-labeled neurons and neurons labeled only with GFP, respectively.

(H) Illustration of the location of the striatum depicted in a coronal section.

(I) A coronal GFP-stained section including the striatum (Marmo2). Scale bar = 1 mm.

(J and K) A high-magnification image of the striatum (arrowheads in I) in the contralateral side (J) and ipsilateral side presenting GFP expression (K). Scale bar = 200 μm. mKO, monomeric Kusabira Orange. TH, tyrosine hydroxylase.

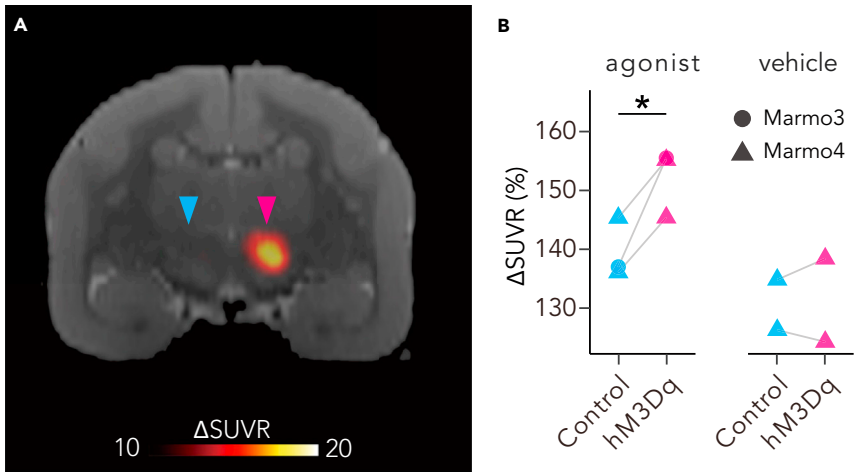

Figure 2. In vivo evaluation of chemogenetic activation of unilateral nigrostriatal dopaminergic (DA) neuron function

(A) A coronal section of parametric image displaying an increase in the standardized uptake value ratio (ΔSUVR) of [^{18}F] fluorodeoxyglucose (FDG) following deschloroclozapine DCZ administration (3 μg/kg intravenous [IV]) overlaying a magnetic resonance image in Marmo4. Red and blue arrowheads indicate the hM3Dq-expressing substantia nigra and its contralateral control side, respectively.

(B) SUVR values of [^{18}F]FDG uptake in the hM3Dq-expressing SN (hM3Dq) and contralateral control SN (control) following agonist and vehicle administration. CNO and DCZ were used as agonist for Marmo3 and 4, respectively. Asterisk indicates a significant difference ($p < 0.05$, Tukey HSD test).

agonist DCZ (Nagai et al., 2020), as DREADD actuators. To monitor DREADD-induced neuronal activation in vivo, we performed PET with [^{18}F]fluorodeoxyglucose (FDG) following intravenous (IV) administration of the actuators to detect a change in regional brain glucose metabolism, an index of brain neuronal excitability (Yokoyama et al., 2012; Reivich et al., 1979; Alexander et al., 2019; Yokoyama and Onoe, 2015). Following the administration of both DCZ and CNO, [^{18}F]FDG uptake was consistently increased on the hM3Dq-expressing side of the SN, with a significant difference from that on the contralateral control side ($p = 0.04$, diff = 12.6, lower = 1.32, upper = 23.78; Tukey HSD test; Figure 2), likely reflecting the increased metabolic activity of hM3Dq-expressing neurons. No comparable lateralized uptake was found in the other areas. These results suggest that activation of the unilateral nigrostriatal DA neurons can be induced by DCZ administration via an excitatory DREADD.

Minimally invasive and reversible control of unilateral DA neurons induced rotation behavior

Having successfully applied chemogenetic excitation of the unilateral nigrostriatal DA neurons, we next examined its effects on the behavior of conscious marmosets. Taking advantage of the effective brain permeability of DCZ, we adopted two routes of systemic administration for behavioral experiments: IP and PO. We expected that IP delivery would provide a relatively rapid effect because of its better absorption, whereas PO delivery offers the benefit of stress- and pain-free operation. Prior to behavioral experiments, we performed pharmacokinetics analysis. Following IP administration (100 μg/kg), serum DCZ concentrations rapidly increased, peaking after 26.2 ± 7.5 min, whereas PO administration (100 μg/kg) resulted in a slower increase in serum DCZ levels, which peaked after 97.5 ± 45 min ($N = 4$, $p = 0.017$, BM Statistic = 4.1, df = 3.65, Brunner–Munzel test for median values; Figure 3). In both cases, the peak DCZ concentration (50–100 nM) was comparable or even higher than that observed in macaque monkeys following the intramuscular injection of DCZ at the same dose (Nagai et al., 2020). Considering the effective dose for hM3Dq for macaques (>1 μg/kg) (Nagai et al., 2020), we selected 3–10 μg/kg as the DCZ doses for subsequent behavioral experiments.

We then tested the non-invasive chemogenetic control of the unilateral dopaminergic system in freely moving marmosets (N = 3; Marmo1, 2, and 4; Table 1). Each marmoset was placed in a Plexiglas cylinder chamber and given a piece of food containing DCZ solution (10 μg/kg) or vehicle. All marmosets voluntarily ate the food immediately upon receipt (Video S1). Approximately 30 min after eating the DCZ-containing

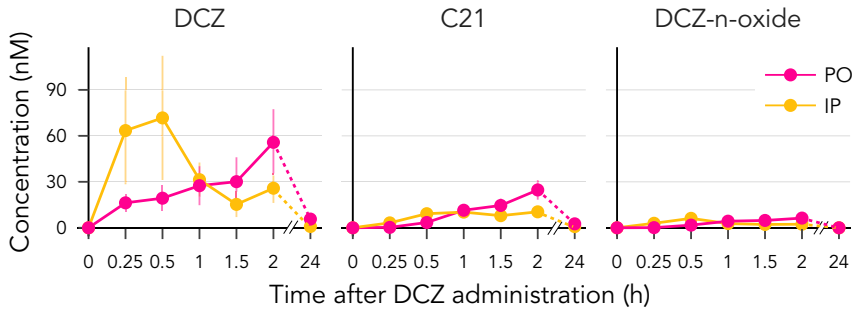

Figure 3. Time–concentration profiles of deschloroclozapine (DCZ) and its metabolites in plasma (DCZ 100 μg/kg per os [PO] or intraperitoneal [IP], mean ± SEM, N = 4).

food, the marmosets began to exhibit head turning, and they eventually rotated in a contralateral direction to the hM3Dq-positive side (Video S2). This contralateral rotation was observed in all three marmosets repeatedly and consistently following DCZ consumption.

To quantify the behavioral alterations, we developed a three-dimensional (3D) motion tracking system (MTS) consisting of four depth cameras (Figures 4A–4D). Briefly, the MTS enables recording of marmoset free motion and its reconstruction as high-resolution 3D point clouds (<3-mm isovoxel) utilizing frame-by-frame parametric physical stimulation, measuring the trajectories of body parts (*Head*, *Body*, *Neck*, and *Hip*) without body markers (Figure 4; see STAR Methods). MTS visualized DCZ induced behavioral changes of the marmosets. Figure 5A presents a typical example of a top view of *Head* trajectory following vehicle and DCZ treatment (PO) and 24 hr after DCZ treatment in a marmoset (Marmo2). After vehicle treatment, the marmoset exhibited "stop-and-go" behavior, as indicated by sparse 'dotted chain' patterns of *Head* trajectory (Figure 5A, left). Following DCZ administration, the marmoset displayed rotation behavior, as represented by a 'tangled ball of yarn'-like *Head* trajectory (Figure 5A, middle). Twenty-four hours after administration, the marmoset displayed a similar movement pattern as observed in the vehicle treatment sessions (Figure 5A right). We also found that following DCZ administration, the marmosets continuously deviated their heads contralaterally to the hM3Dq-positive side relative to the body axis. To quantify this behavioral change, we analyzed the shifts of the *Head* and *Hip* positions (Figure 5B). The scatterplots revealed the contralateral deviation of the *Head* position and *Hip* deviation to the opposite side, which specifically occurred 45–60 min after DCZ administration (Figure 5B, right). The contralateral deviation was consistently observed in the two other marmosets (Figure S1).

Using MTS measurement, we compared the behavioral effects following PO and IP administration in two marmosets (Marmo1 and 2). Both marmosets repeatedly and selectively exhibited contralateral rotation following DCZ administration. Both IP and PO DCZ administration significantly increased horizontal *Head* velocity ($p = 9.8 \times 10^{-4}$, F[2,21] = 13.64, two-way ANOVA, Figure 5C) but not vertical velocity (p = 0.98, F [2,21] = 0.023, two-way ANOVA). We quantified the degree of marmoset body rotation by measuring the sum of rotation of the horizontal body axis (θ_{rot}, Figure 5D). We found that the frequency of contralateral rotation was significantly higher following DCZ administration than after vehicle administration and at 24 hr after DCZ administration (DCZ vs. vehicle, p = 0.0018, diff. = 1.87; DCZ vs. post, p = 0.0012, diff. = 1.94; vehicle vs. post, p = 0.99, diff. = 0.07, Tukey's HSD test, F[2,21] = 11.3, Figure 5D). We also examined the temporal dynamics of the behavioral change by calculating the cumulative sum of rotation in 5-min windows. As presented in Figure 5E, Marmo2 exhibited contralateral *Head* orientation bias 30–60 min after oral DCZ administration (yellow-green lines in Figure 5E). This bias disappeared after 24 hr but reappeared after the second DCZ dose. We defined the latency of significant behavioral changes as the timing at which the cumulative sum of θ_{rot} deviated from the 95% confidence intervals of those in vehicle-treated sessions (Figure 5F). The latency of behavioral change was shorter in the IP sessions (15 ± 7 min) than in the PO sessions (45.6 ± 15.5 min; p = 0.004, F[1,6] = 24.3, two-way ANOVA, Figure 5G), likely reflecting rapid absorption of the IP-delivered drug and high DCZ availability in blood (Figure 3). Contralateral rotation was continuously observed until the end of the testing session (approximately 90 min), resulting in significantly more rotations than in vehicle-treated sessions (p = 0.003, F [1,12] = 14.0, repeated-measures one-way ANOVA; Figure S1C). There were no significant differences

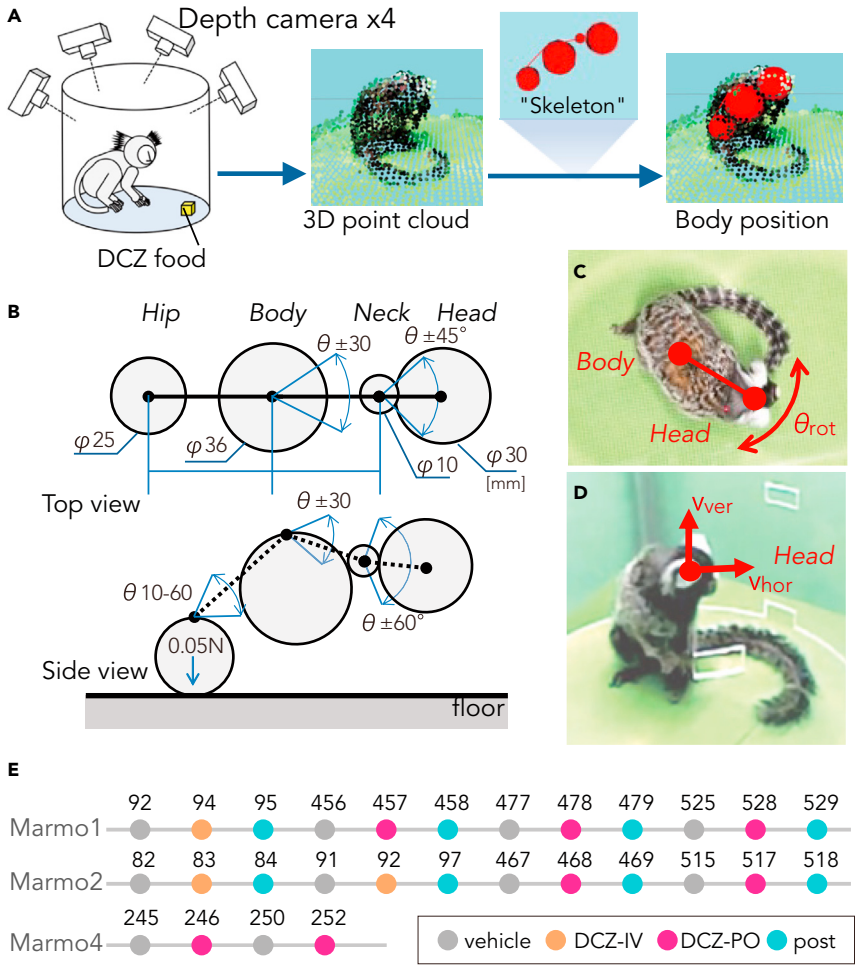

Figure 4. Markerless 3D motion tracking system (MTS) and experimental design of the behavioral test

(A) Illustration of the analytical data flow of MTS. The positions of animal body parts, namely *Head*, *Neck*, *Body*, and *Hip*, were estimated through a statistical skeleton model that simulated the full three-dimensional point cloud of the marmoset body surface extracted from four depth cameras.

(B) Schematics of a marmoset body skeleton model. Arrows represent the part sizes, attraction force between *Hip* and floor, and the range of movement of joints.

(C) Body rotation speed (θ_{rot}) was the angular speed of the horizontal *Body–Head* axis.

(D) *Head* movement was divided into horizontal (V_{hor}) and vertical vectors (V_{ver}).

(E) Experimental schedule. Marmo1 and 2 were examined under conditions (vehicle treatment, deschloroclozapine (DCZ) treatment, and 24 hr after DCZ treatment) using a repeated-measures design with a total of four repetitions of either per os [PO] or intraperitoneal [IP] administration. Marmo4 was examined under vehicle and DCZ-PO administrations. The numbers represent the days after vector injection.

in the peak rotation numbers per 10 min between PO and IP (i.e., peak values in Figure 5F; $p = 0.16$), suggesting that the intensities of the behavioral effects were comparable. By contrast, non-DREADD-expressing marmosets did not display altered *Head* trajectories or *Head* deviations following DCZ administration (N = 2; Figure S2), suggesting that the behavioral changes in the hM3Dq-expressing marmosets were attributable to chemogenetic activation.

DISCUSSION

Using DREADDs, we demonstrated that temporal activation of the unilateral nigrostriatal DA system induced contralateral rotation behavior in the common marmosets. To the best of our knowledge, this is the first study to demonstrate chemogenetic control of neuronal activity and behavioral action in common

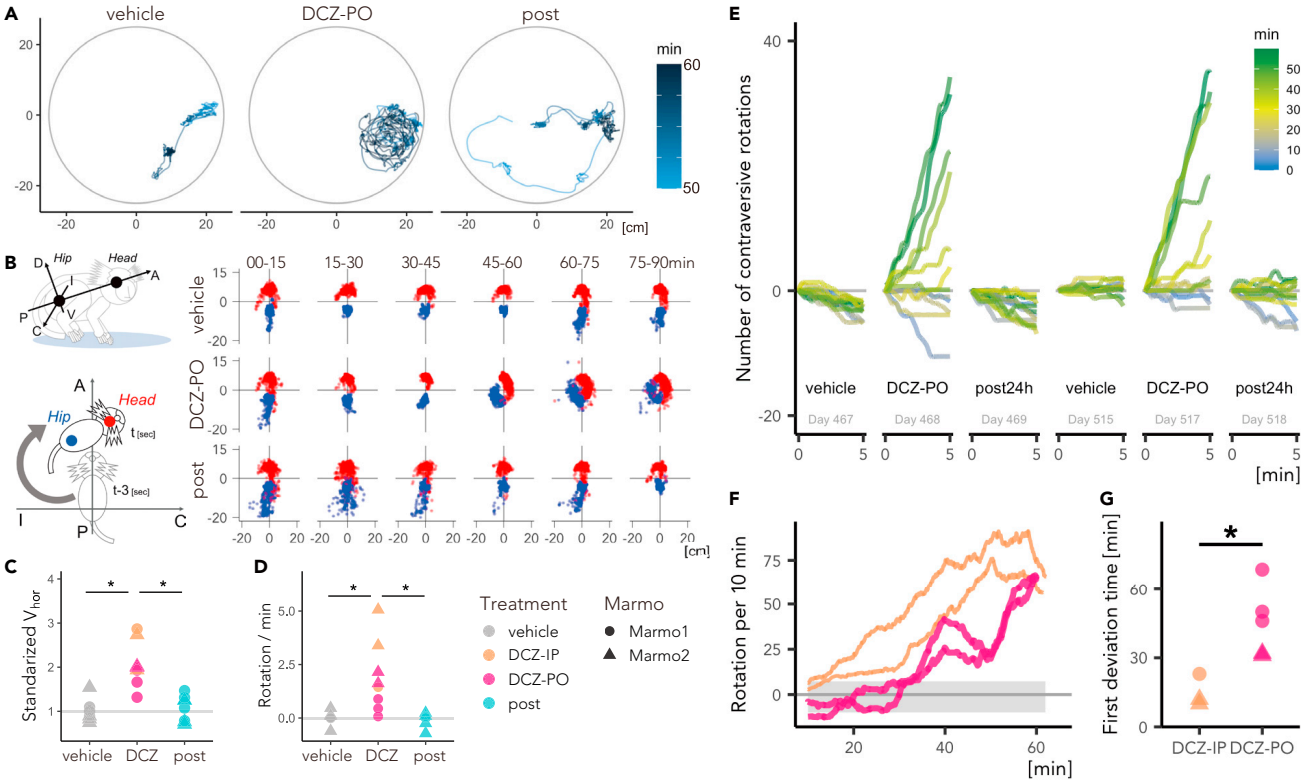

Figure 5. Chemogenetic activation of unilateral substantia nigra (SN) drives contralateral rotation behavior

(A) Example of the top view of the *Head* trajectory of Marmo1 50–60 min after vehicle and deschloroclozapine (DCZ; 10 μg/kg, per os [PO]) administration and 24 hr after DCZ administration.

(B) Postural changes characterized by the positions of the *Head* and *Body* relative to the body axis. *Left top*: The body axis, i.e., the anterior–posterior (A–P) axis, is defined as that through the center of the *Head* and *Body*, whereas the ipsilateral-contralateral (I-C) and dorsal-ventral (D-V) axes are defined as those horizontally and vertically orthogonal to the A-P axis. *Left bottom*: Relative *Head* and *Hip* positions were determined every 3 s in the A–P I–C plane. *Right*: Scatterplots of the *Head* (red) and *Hip* (blue) positions over a 15-min period following vehicle and DCZ (PO) administration and 24 hr after DCZ administration (Marmo1).

(C) Comparison of the average horizontal *Head* speed (V_{hor}) scaled per individual with the vehicle conditions equal to 1 in animals treated with vehicle and DCZ (blue: IP; red: PO), and 24 hr after DCZ administration (post) for Marmo1 and Marmo2. (D) Comparison of the average frequency of contralateral rotation among three conditions.

(E) Representative trends of the cumulative sum of the contraversive rotation every 5 min across conditions in Marmo2. Color scale representing the time after the treatment/test start.

(F) Total number of contraversive rotations for every sliding 10-min window for IP (blue) and PO DCZ treatment (red) in Marmo2. Gray shadow represents the 95% confidence intervals of the cumulative sum of θ_{rot} under the vehicle condition.

(G) Comparison of the latency of significant behavioral changes between IP and PO DCZ treatment, which was defined as the first deviation time from the 95% confidence interval of those under the vehicle condition. Asterisks indicate a significant difference ($p < 0.01$, two-way ANOVA). See also Figures S1 and S2.

marmosets. A combination of our experimental methods employed in this study, including (1) imaging-guided viral vector delivery, (2) in vivo monitoring of DREADD expression and function, (3) painless and stress-free delivery of DREADD actuator, and (4) markerless motion tracking analysis, was critical to our successful chemogenetic manipulation and behavioral analysis in marmosets under freely moving conditions.

The specific delivery of transgenes is a critical step for successful chemogenetic manipulation, especially for deep brain structures. The use of non-invasive imaging methods, such as magnetic resonance imaging (MRI) and CT, has been proposed for assessment of the injection site even during surgery (Schumacher et al., 1992; Hampton et al., 2004). The present study used CT to visualize the injection cannula (33 gauge/210 μm diameter) with 80-μm spatial resolution. Intraoperative CT was successfully used to adjust the position of the injection cannula to the target at the co-registered MR image, helping to localize hM3Dq expression at the SN. To manipulate the nigrostriatal neurons, we first used two AAV vector

constructs, namely, AAV2-CMV-hM3Dq and AAV2.1-hSyn1-hM3Dq-IRES-AcGFP (Table 1), both of which confer neuron-specific expression (Yaguchi et al., 2013; Kügler et al., 2003; Kimura et al., 2021). Even without a DA-specific expression system, histological confirmation indicated that hM3Dq was successfully expressed in the DA neurons in the SNc (Figure 1G). Because of the lack of specificity and a relatively large-volume injection, GFP-positive neurons were also found outside the SN. We additionally used a DA neuron-specific, TH promoter (Stauffer et al., 2016), with a smaller injection volume to increase the specificity of the transgene in a marmoset (Marmo4). Despite the use of different expression systems, our model displayed in vivo hM3Dq expression in the SN that was confirmed by immunohistochemistry, thus allowing us to conduct the chemogenetic manipulation of marmoset behavior.

Prior to testing the behavioral effect of DREADD activation, it is useful to clarify designer receptor expression and function. In previous studies, PET using radiolabeled DREADD agonists was used to visualize the site and level of expression of hM4Di/hM3Dq in living rodents and macaques (Nagai et al., 2016; Nagai et al., 2020; Ji et al., 2016; Gomez et al., 2017; Bonaventura et al., 2019). In the present study, we performed PET using [^{11}C]DCZ, a selective radioligand validated in hM3Dq-expressing mice and macaques (Nagai et al., 2020). We visualized hM3Dq expression as increased tracer binding specifically at the target location in all four marmosets, which was consistent with the in vitro immunohistochemical data. We also used PET to monitor the functional effects of DREADDs. Glucose metabolism was measured using [^{18}F]FDG as an in vivo representation of neuronal activity (Michaelides et al., 2013). Increased [^{18}F]FDG uptake was significantly observed in hM3Dq-expressing regions following agonist administration, indicating chemogenetic activation of the SN. Our data indicate that the combination of chemogenetics with non-invasive imaging methods should be valuable for future translational studies toward the development and validation of therapeutic methodologies as, for example, cell replacement therapy of Parkinson's disease (Dell'Anno et al., 2014).

When examining chemogenetic effects on behavior, it is critical to minimize the adverse side effects of agonist administration itself. Conventional administration routes such as IP may cause pain and stress in the subjects. Previous DREADD studies in rodents used non-invasive CNO delivery through drinking water or food (Wess et al., 2013; Urban et al., 2016; Padilla et al., 2017; Fernandez et al., 2018). Although the timing and dose are less precise and controllable, PO delivery of CNO has proven useful for chronic chemogenetic manipulation. In the current study, we used DCZ, a highly potent DREADD agonist with better brain permeability than CNO and C21 (Nagai et al., 2020). Because the effective dose of DCZ is approximately 1% of that of CNO, the solution volume (approximately 0.1 mL) was sufficiently small to permit its addition to food. Because the animals always ate the DCZ- or vehicle-containing food immediately, PO administration is an optimal non-invasive agonist delivery method for marmosets with better control of dose and timing. Indeed, our results indicated that the PO delivery of DCZ induced behavioral changes in marmosets via hM3Dq, in line with the results following IP injections. Further, we believe that our PO protocols are also beneficial and applicable to long-lasting or chronic DREADD manipulation in marmosets.

Unlike CNO, the metabolites of which cause off-target effects, DCZ does not produce brain-permeable metabolites in mice and macaques (Nagai et al., 2020). Our pharmacokinetic analysis in marmosets indicated that C21, a metabolite of DCZ, accumulated in plasma to a certain amount. Because C21 displays weak brain permeability, the effects of converted C21 on DREADDs should be negligible. Although no significant effect of DCZ (10 μg/kg PO) and its metabolites on movement speed and direction was found in non-DREADD subjects (Figure S2), potential off-target effects should be considered in future studies in marmosets using an inhibitory DREADD, which may require higher DCZ doses.

It has repeatedly been demonstrated that contralateral rotation behavior is induced by activating the unilateral nigrostriatal system via electrical stimulation or the intrastriatal injection of DA releasers in rats (Smith et al., 1996; van der Heyden, 1984; Arbuthnott and Ungerstedt, 1975). In accordance, the current study demonstrated that chemogenetic activation of unilateral nigrostriatal DA neurons induced rotation behavior contralaterally to the activated side in marmosets. As mentioned previously, chemogenetic activation was not necessarily induced in DA neurons exclusively, because hM3Dq expression was detected in some neurons outside the SNc, including SN pars reticulata (SNr) neurons. Hence, chemogenetic activation of these off-target neurons might have contributed to the observed behavioral changes. However, excitation of SNr neurons would result in ipsiversive rotation behavior (Kravitz

et al., 2010; Alcacer et al., 2017), and therefore its contribution to our model may be minor. Taken together, the most plausible explanation for the observed rotation behavior is the result of chemogenetic activation of DA neurons in SNc.

Although the behavioral alterations in our study were apparent and easily detected via visual inspection (Video S2), objective quantification is critical for reproducibility and deep understanding of the behavioral consequences of chemogenetic manipulation. In particular, the posture of animals — a series of movements of the major body parts — reflects both motor function and their internal state such as emotion and intention (Dael et al., 2012; Coulson, 2004; Matsumoto et al., 2013, 2014; Mimura et al., 2015; Nakamura et al., 2016). Conventional systems available for marmosets focus on simple macroscale parameters (e.g., circadian activity rhythms (Yabumoto et al., 2019)) or a few microbehavioral parameters (e.g., eye and face orientation (Brattain et al., 2016; Turesson et al., 2016)). We developed a markerless MTS that tracks and digitizes the 3D trajectory of the major body parts of marmosets, thereby reconstructing and analyzing the sequence of posture. Our results indicated that the MTS provides a powerful means for visualizing and quantifying the effects of chemogenetic activation of the DA neurons in a data-driven manner.

One shortcoming of our system was the relatively high computation costs of the measurement and calculation processes, which were not fully automated but were divided into several sub-processes because of the large amount of data (approximately 20 GB per 30 min). Thus, real-time detection of specific behavioral events remains a challenge for future work. We are currently extending this system to examine two marmosets simultaneously, making it feasible for future chemogenetic studies of social interactions.

In summary, using hM3Dq and oral DCZ administration, we manipulated the nigrostriatal DA neurons in freely behaving marmosets. We also demonstrated the utility of non-invasive imaging methods for validating DREADD expression and assessing the functional effects of DREADDs. Our results confirmed that the activity of a specific neuronal population can be controlled in marmosets for hours. A novel markerless MTS allowed analyses of multiparametric body part motion and quantification of the behavioral alterations. Collectively, these chemogenetic methods will broaden the utility of the marmoset as a primate model for clarifying the neurobiological mechanisms of emotion, cognition, and social functions and developing novel therapeutic approaches to psychiatric and neurological diseases.

Limitations of the study

- Limitations of this study regarding the DA-neuron specificity of hM3Dq expression are discussed above. Although consistent chemogenetic behavioral effects were obtained using different expression systems, future studies should take advantage of DA-neuron specific promoters.
- Along with contralateral rotation quantified as head deviation (shift of position relative to the body axis), the marmosets frequently rotated their heads contralaterally. However, the current MTS system is not capable of measuring such head motions. For future studies, we plan to update MTS to detect and track face orientation, which may be important measures for evaluating higher-order behavioral expressions.

STAR★METHODS

Detailed methods are provided in the online version of this paper and include the following:

- KEY RESOURCES TABLE
- RESOURCE AVAILABILITY
  - Lead contact
  - Materials availability
  - Data and code availability
- EXPERIMENTAL MODEL AND SUBJECT DETAILS
  - Animals
- METHOD DETAILS
  - Viral vector production
  - Surgery and vector injection
  - Drug administration
  - PET

- Histology
- Behavioral testing
- Markerless 3D MTS
- MRI and CT
- Pharmacokinetics analysis

- QUANTIFICATION AND STATISTICAL ANALYSIS
  - PET data analysis
  - Behavioral data analysis

SUPPLEMENTAL INFORMATION

Supplemental information can be found online at https://doi.org/10.1016/j.isci.2021.103066.

ACKNOWLEDGMENTS

We thank J. Kamei, R. Yamaguchi, Y. Matsuda, Y. Sugii, T. Kokufuta, A. Maruyama, Y. Iwasawa, A. Tanizawa, S. Shibata, N. Nitta, M. Nakano, and M. Fujiwara for their technical assistance. We also thank Dr. M-R. Zhang and his colleagues at Department of Radiopharmaceuticals Development, QST for producing the radioligands. This study was supported by MEXT/JSPS KAKENHI Grant Numbers JP17H06040, JP19H04996 (to KM), and JP17H02219 (TH), JP18H04037 (to TM), and AMED under Grant Numbers JP20dm0307021 (to KI), JP21dm0307007 (to TH), JP21dm0207003 (to MT), JP20dm0307026 (to CS), and JP21dm0207072 (to MH), and JP21dm0107146 (to TM).

AUTHOR CONTRIBUTIONS

Conceptualization, T.M; formal analysis, K.M., Y.N., and T.O.; investigation, K.M., Y.N., K.I., and Y.H.; resources, K.I. and J.M.; writing (original draft), K.M. and T.M.; visualization, K.M. and Y.N.; supervision, T.S., M.T., M.H., and T.M.; project administration, T.M.; funding acquisition, K.M., T.H., K.I., M.T., T.S., M.H., and T.M.; writing (review and editing), all authors.

DECLARATION OF INTERESTS

The authors declare no competing interests.

Received: May 22, 2021
Revised: July 19, 2021
Accepted: August 26, 2021
Published: September 24, 2021

REFERENCES

Alcacer, C., Andreoli, L., Sebastianutto, I., Jakobsson, J., Fieblinger, T., and Cenci, M.A. (2017). Chemogenetic stimulation of striatal projection neurons modulates responses to Parkinson's disease therapy. J. Clin. Invest. *127*, 720–734. https://doi.org/10.1172/JCI90132.

Alexander, G.M., Rogan, S.C., Abbas, A.I., Armbruster, B.N., Pei, Y., Allen, J.A., Nonneman, R.J., Hartmann, J., Moy, S.S., Nicolelis, M.A., et al. (2009). Remote control of neuronal activity in transgenic mice expressing evolved G protein-coupled receptors. Neuron *63*, 27–39. https://doi.org/10.1016/j.neuron.2009.06.014.

Alexander, L., Gaskin, P.L.R., Sawiak, S.J., Fryer, T.D., Hong, Y.T., Cockcroft, G.J., Clarke, H.F., and Roberts, A.C. (2019). Fractionating blunted reward processing characteristic of anhedonia by over-activating primate subgenual anterior cingulate cortex. Neuron *101*, 307–320.e6. https://doi.org/10.1016/j.neuron.2018.11.021.

Ando, K., Obayashi, S., Nagai, Y., Oh-Nishi, A., Minamimoto, T., Higuchi, M., Inoue, T., Itoh, T., and Suhara, T. (2012). PET analysis of dopaminergic neurodegeneration in relation to immobility in the MPTP-treated common marmoset, a model for Parkinson's disease. PLoS One *7*, 3–10. https://doi.org/10.1371/journal.pone.0046371.

Arbuthnott, G.W., and Ungerstedt, U. (1975). Turning behavior induced by electrical stimulation of the nigro-neostriatal system of the rat. Exp. Neurol. *47*, 162–172. https://doi.org/10.1016/0014-4886(75)90244-7.

Ausderau, K.K., Dammann, C., McManus, K., Schneider, M., Emborg, M.E., and Schultz-Darken, N. (2017). Cross-species comparison of behavioral neurodevelopmental milestones in the common marmoset monkey and human child. Dev. Psychobiol. *59*, 807–821. https://doi.org/10.1002/dev.21545.

Bonaventura, J., Eldridge, M.A.G., Hu, F., Gomez, J.L., Sanchez-Soto, M., Abramyan, A.M., Lam, S., Boehm, M.A., Ruiz, C., Farrell, M.R., et al. (2019). High-potency ligands for DREADD imaging and activation in rodents and monkeys. Nat. Commun. *10*, 1–12. https://doi.org/10.1038/s41467-019-12236-z.

Brattain, L.J., Landman, R., Johnson, K.A., Chwalek, P., Hyman, J., Jennings, C., Desimone, R., Feng, G., and Quatieri, T.F. (2016). A multimodal sensor system for automated marmoset behavioral analysis. IEEE 13th Int. Conf. Wearable Implant. Body Sens. Netw. (Bsn), 254–259. https://doi.org/10.1109/BSN.2016.7516269.

Clarke, H.F., Hill, G.J., Robbins, T.W., and Roberts, A.C. (2011). Dopamine, but not serotonin, regulates reversal learning in the marmoset caudate nucleus. J. Neurosci. *31*, 4290–4297. https://doi.org/10.1523/JNEUROSCI.5066-10.2011.

Coulson, M. (2004). Attributing emotion to static body postures: recognition accuracy, confusions, and viewpoint dependence. J. Nonverbal Behav. *28*, 117–139. https://doi.org/10.1023/B:JONB.0000023655.25550.be.

Dael, N., Mortillaro, M., and Scherer, K.R. (2012). Emotion expression in body action and posture. Emotion *12*, 1085–1101. https://doi.org/10.1037/a0025737.

Dell'Anno, M.T., Caiazzo, M., Leo, D., Dvoretskova, E., Medrihan, L., Colasante, G., Giannelli, S., Theka, I., Russo, G., Mus, L., Pezzoli, G., Gainetdinov, R.R., Benfenati, F., Taverna, S., Dityatev, A., and Broccoli, V. (2014). Remote control of induced dopaminergic neurons in parkinsonian rats. J. Clin. Invest. *124*, 3215–3229. https://doi.org/10.1172/JCI74664.

Eldridge, M.A., Lerchner, W., Saunders, R.C., Kaneko, H., Krausz, K.W., Gonzalez, F.J., Ji, B., Higuchi, M., Minamimoto, T., and Richmond, B.J. (2016). Chemogenetic disconnection of monkey orbitofrontal and rhinal cortex reversibly disrupts reward value. Nat. Neurosci. *19*, 37–39. https://doi.org/10.1038/nn.4192.

Fernandez, D.C., Fogerson, P.M., Lazzerini Ospri, L., Thomsen, M.B., Layne, R.M., Severin, D., Zhan, J., Singer, J.H., Kirkwood, A., Zhao, H., et al. (2018). Light affects mood and learning through distinct retina-brain pathways. Cell *175*, 71–84.e18. https://doi.org/10.1016/j.cell.2018.08.004.

Gomez, J.L., Bonaventura, J., Lesniak, W., Mathews, W.B., Sysa-Shah, P., Rodriguez, L.A., Ellis, R.J., Richie, C.T., Harvey, B.K., Dannals, R.F., et al. (2017). Chemogenetics revealed: DREADD occupancy and activation via converted clozapine. Science *357*, 503–507. https://doi.org/10.1126/science.aan2475.

Hampton, R.R., Buckmaster, C.A., Anuszkiewicz-Lundgren, D., and Murray, E.A. (2004). Method for making selective lesions of the hippocampus in macaque monkeys using NMDA and a longitudinal surgical approach. Hippocampus *14*, 9–18. https://doi.org/10.1002/hipo.10150.

Horst, N.K., Jupp, B., Roberts, A.C., and Robbins, T.W. (2019). D2 receptors and cognitive flexibility in marmosets: tri-phasic dose-response effects of intra-striatal quinpirole on serial reversal performance. Neuropsychopharmacology *44*, 564–571. https://doi.org/10.1038/s41386-018-0272-9.

Ichise, M., and Ballinger, J.R. (1996). From graphical analysis to multilinear regression analysis of reversible radioligand binding. J. Cereb. Blood Flow Metab. *16*, 750–752. https://doi.org/10.1097/00004647-199607000-00028.

Ji, B., Kaneko, H., Minamimoto, T., Inoue, H., Takeuchi, H., Kumata, K., Zhang, M.R., Aoki, I., Seki, C., Ono, M., et al. (2016). Multimodal imaging for DREADD-expressing neurons in living brain and their application to implantation of iPSC-derived neural progenitors. J. Neurosci. *36*, 11544–11558. https://doi.org/10.1523/JNEUROSCI.1279-16.2016.

Kimura, K., Nagai, Y., Hatanaka, G., Fang, Y., Tanabe, S., Zheng, A., Fujiwara, M., Nakano, M., Hori, Y., Takeuchi, R., et al. (2021). A mosaic adeno-associated virus vector as a versatile tool that exhibits high levels of transgene expression and neuron specificity in primate brain. bioRxiv. https://doi.org/10.1101/2021.07.18.452859.

Koshiba, M., Mimura, K., Sugiura, Y., Okuya, T., Senoo, A., Ishibashi, H., and Nakamura, S. (2011). Reading marmoset behavior "semantics" under particular social context by multi-parameters correlation analysis. Prog. Neuro-Psychopharmacol. Biol. Psychiatry *35*, 1499–1504. https://doi.org/10.1016/j.pnpbp.2011.01.021.

Kravitz, A.V., Freeze, B.S., Parker, P.R.L., Kay, K., Thwin, M.T., Deisseroth, K., and Kreitzer, A.C. (2010). Regulation of parkinsonian motor behaviours by optogenetic control of basal ganglia circuitry. Nature *466*, 622–626. https://doi.org/10.1038/nature09159.

Kügler, S., Kilic, E., and Bähr, M. (2003). Human synapsin 1 gene promoter confers highly neuron-specific long-term transgene expression from an adenoviral vector in the adult rat brain depending on the transduced area. Gene Ther. *10*, 337–347. https://doi.org/10.1038/sj.gt.3301905.

Matsumoto, J., Urakawa, S., Takamura, Y., Malcher-Lopes, R., Hori, E., Tomaz, C., Ono, T., and Nishijo, H. (2013). A 3D-video-based computerized analysis of social and sexual interactions in rats. PLoS One *8*, e78460. https://doi.org/10.1371/journal.pone.0078460.

Matsumoto, J., Uehara, T., Urakawa, S., Takamura, Y., Sumiyoshi, T., Suzuki, M., Ono, T., and Nishijo, H. (2014). 3D video analysis of the novel object recognition test in rats. Behav. Brain Res. *272*, 16–24. https://doi.org/10.1016/j.bbr.2014.06.047.

Michaelides, M., Anderson, S.A.R., Ananth, M., Smirnov, D., Thanos, P.K., Neumaier, J.F., Wang, G.-J., Volkow, N.D., and Hurd, Y.L. (2013). Whole-brain circuit dissection in free-moving animals reveals cell-specific mesocorticolimbic networks. J. Clin. Invest. *123*, 5342–5350. https://doi.org/10.1172/JCI72117.

Miller, C.T., Freiwald, W.A., Leopold, D.A., Mitchell, J.F., Silva, A.C., and Wang, X. (2016). Marmosets: a neuroscientific model of human social behavior. Neuron *90*, 219–233. https://doi.org/10.1016/j.neuron.2016.03.018.

Mimura, K., Kishino, H., Karino, G., Nitta, E., Senoo, A., Ikegami, K., Kunikata, T., Yamanouchi, H., Nakamura, S., Sato, K., and Koshiba, M. (2015). Potential of a smartphone as a stress-free sensor of daily human behaviour. Behav. Brain Res. *276*, 181–189. https://doi.org/10.1016/j.bbr.2014.06.007.

Mitchell, J.F., and Leopold, D.A. (2015). The marmoset monkey as a model for visual neuroscience. Neurosci. Res. *93*, 20–46. https://doi.org/10.1016/j.neures.2015.01.008.

Nagai, Y., Kikuchi, E., Lerchner, W., Inoue, K.-I., Ji, B., Eldridge, M.A.G., Kaneko, H., Kimura, Y., Oh-Nishi, A., Hori, Y., et al. (2016). PET imaging-guided chemogenetic silencing reveals a critical role of primate rostromedial caudate in reward evaluation. Nat. Commun. *7*, 13605. https://doi.org/10.1038/ncomms13605.

Nagai, Y., Miyakawa, N., Takuwa, H., Hori, Y., Oyama, K., Ji, B., Takahashi, M., Huang, X.-P., Slocum, S.T., DiBerto, J.F., et al. (2020). Deschloroclozapine, a potent and selective chemogenetic actuator enables rapid neuronal and behavioral modulations in mice and monkeys. Nat. Neurosci. *23*, 1157–1167. https://doi.org/10.1038/s41593-020-0661-3.

Nakamura, T., Matsumoto, J., Nishimaru, H., Bretas, R.V., Takamura, Y., Hori, E., Ono, T., and Nishijo, H. (2016). A markerless 3D computerized motion capture system incorporating a skeleton model for monkeys. PLoS One *11*, e0166154. https://doi.org/10.1371/journal.pone.0166154.

Padilla, S.L., Qiu, J., Nestor, C.C., Zhang, C., Smith, A.W., Whiddon, B.B., Rønnekleiv, O.K., Kelly, M.J., and Palmiter, R.D. (2017). AgRP to Kiss1 neuron signaling links nutritional state and fertility. Proc. Natl. Acad. Sci. U. S. A. *114*, 2413–2418. https://doi.org/10.1073/pnas.1621065114.

Reivich, M., Kuhl, D., and Wolf, A. (1979). The [^{18}F] fluorodeoxyglucose method for the measurement of local cerebral glucose utilization in man. Circ. Res. *44*, 127–137. https://doi.org/10.1161/01.RES.44.1.127.

Roth, B.L. (2017). DREADDs for neuroscientists. Neuron *89*, 683–694. https://doi.org/10.1016/j.neuron.2016.01.040.DREADDs.

Schumacher, J.M., Hantraye, P., Brownell, A.L., Riche, D., Madras, B.K., Davenport, P.D., Maziere, M., Elmaleh, D.R., Brownell, G.L., and Isacson, O. (1992). A primate model of Huntington's disease: functional neural transplantation and CT-guided stereotactic procedures. Cell Transplant. *1*, 313–322. https://doi.org/10.1177/096368979200100409.

Smith, L., De Salvia, M., Jenner, P., and Marsden, C.D. (1996). An appraisal of the antiparkinsonian activity of piribedil in 1-methyl-4-phenyl-1,2,3,6-tetrahydropyridine-treated common marmosets. Mov. Disord. *11*, 125–135. https://doi.org/10.1002/mds.870110203.

Stauffer, W.R., Lak, A., Yang, A., Borel, M., Paulsen, O., Boyden, E.S., and Schultz, W. (2016). Dopamine neuron-specific optogenetic stimulation in Rhesus macaques. Cell *166*, 1564–1571.e6. https://doi.org/10.1016/j.cell.2016.08.024.

Suzuki, W., Banno, T., Miyakawa, N., Abe, H., Goda, N., and Ichinohe, N. (2015). Mirror neurons in a new world monkey, common marmoset. Front. Neurosci. *9*, 459. https://doi.org/10.3389/fnins.2015.00459.

Takahashi, D.Y., Liao, D.A., and Ghazanfar, A.A. (2017). Vocal learning via social Reinforcement by infant marmoset monkeys. Curr. Biol. *27*, 1844–1852.e6. https://doi.org/10.1016/j.cub.2017.05.004.

Takaji, M., Takemoto, A., Yokoyama, C., Watakabe, A., Mizukami, H., Ozawa, K., Onoe, H., Nakamura, K., and Yamamori, T. (2016). Distinct roles for primate caudate dopamine D1 and D2 receptors in visual discrimination learning revealed using shRNA knockdown. Sci. Rep. *6*, 1–16. https://doi.org/10.1038/srep35809.

Turesson, H., Conceição, T.B.R., and Ribeiro, S. (2016). Head and gaze tracking of unrestrained marmosets. BioRxiv. https://doi.org/10.1101/079566.

Upright, N.A., Brookshire, S.W., Schnebelen, W., Damatac, C.G., Hof, P.R., Browning, P.G.F., Croxson, P.L., Rudebeck, P.H., and Baxter, M.G. (2018). Behavioral effect of chemogenetic inhibition is directly related to receptor transduction levels in Rhesus monkeys. J. Neurosci. *38*, 7969–7975. https://doi.org/10.1523/JNEUROSCI.1422-18.2018.

Urban, D.J., Zhu, H., Marcinkiewcz, C.A., Michaelides, M., Oshibuchi, H., Rhea, D., Aryal, D.K., Farrell, M.S., Lowery-Gionta, E., Olsen, R.H.J., et al. (2016). Elucidation of the behavioral program and neuronal network encoded by dorsal raphe serotonergic neurons. Neuropsychopharmacology *41*, 1404–1415. https://doi.org/10.1038/npp.2015.293.

van der Heyden, J.A. (1984). Circling behaviour induced by electrical stimulation of the medial forebrain bundle, importance of stimulus parameters and dopaminergic processes. Pharmacol. Biochem. Behav. *21*, 567–574. https://doi.org/10.1016/s0091-3057(84)80041-6.

Wess, J., Nakajima, K., and Jain, S. (2013). Novel designer receptors to probe GPCR signaling and physiology. Trends Pharmacol. Sci. *34*, 385–392. https://doi.org/10.1016/j.tips.2013.04.006.

Wickham, H., Averick, M., Bryan, J., Chang, W., McGowan, L., François, R., Grolemund, G., Hayes, A., Henry, L., Hester, J., et al. (2019). Welcome to the tidyverse. J. Open Source Softw. *4*, 1686. https://doi.org/10.21105/joss.01686.

Yabumoto, T., Yoshida, F., Miyauchi, H., Baba, K., Tsuda, H., Ikenaka, K., Hayakawa, H., Koyabu, N., Hamanaka, H., Papa, S.M., et al. (2019). MarmoDetector: a novel 3D automated system for the quantitative assessment of marmoset behavior. J. Neurosci. Methods *322*, 23–33. https://doi.org/10.1016/j.jneumeth.2019.03.016.

Yaguchi, M., Ohashi, Y., Tsubota, T., Sato, A., Koyano, K.W., Wang, N., and Miyashita, Y. (2013). Characterization of the properties of seven promoters in the motor cortex of rats and monkeys after lentiviral vector-mediated gene transfer. Hum. Gene Ther. Methods *24*, 333–344. https://doi.org/10.1089/hgtb.2012.238.

Yokoyama, I., Moritan, T., and Inoue, Y. (2012). Functional imaging of skeletal muscle glucose metabolism by [^{18}F]FDG PET to characterize insulin resistance in patients at high risk for coronary artery disease. J. Biomed. Sci. Eng. *05*, 819–825. https://doi.org/10.4236/jbise.2012.512a103.

Yokoyama, C., and Onoe, H. (2015). Positron emission tomography imaging of the social brain of common marmosets. Neurosci. Res. *93*, 82–90. https://doi.org/10.1016/j.neures.2014.12.006.

STAR★METHODS

KEY RESOURCES TABLE

REAGENT or RESOURCE	SOURCE	IDENTIFIER
Antibodies		
Rabbit monoclonal anti-GFP	Thermo Fisher Scientific	Cat# G10362
donkey anti-rabbit IgG antibody	Jackson Laboratories	711-005-152
Bacterial and virus strains		
AAV2.1-hSyn1-hM3Dq-IRES-AcGFP	Kimura et al., 2021	N/A
AAV2.1-TH-hM3Dq-IRES-AcGFP	This paper	N/A
AAV2-CMV-hM3Dq	This paper	N/A
AAV2-CMV-AcGFP	This paper	N/A
AAV2-CMV-mKO	This paper	N/A
AAV2.1-TH- AcGFP	This paper	N/A
Chemicals, peptides, and recombinant proteins		
Deschloroclozapine (DCZ)	MedChemExpress	HY-42110
dimethyl sulfoxide (DMSO)	FUJIFILM Wako Pure Chemical Co.	CAS# 67-68-5
clozapine-N-oxide (CNO)	Toronto Research, Canada	Cat# HY-17366
Diaminobenzine tetrahydrochloride	Fujifilm Wako	Cat# WK04522833
[^{11}C]DCZ	Nagai et al., 2016	N/A
[^{18}F]FDG	Nihon Medi-Physics Co., Ltd.	JAM 4987489900013
Experimental models: Organisms/strains		
Common marmoset	QST	N/A
Critical commercial assays		
Avidin-biotin-peroxidase complex kit	Vector laboratories	Cat# PK-6100
Software and algorithms		
PMOD 4.2	PMOD Technologies	RRID:SCR_016547
3D-MTS	This paper 3DTracker-FAB	3dtracker.org
R version 3.6.1	R core team	r-project.org
tidyverse version 1.3.0	Wickham et al., 2019	tidyverse.org

RESOURCE AVAILABILITY

Lead contact

Further information and requests for resources and reagents should be directed to and will be fulfilled by the lead contact, Takafumi Minamimoto (minamimoto.takafumi@qst.go.jp).

Materials availability

The program sources used in this study are available from the corresponding authors upon reasonable request.

Data and code availability

- All the data supporting the findings of this study have been deposited in a repository (GitHub: https://github.com/minamimoto-lab/2021-Mimura-MarmoDREADD) and are publicly available as of the date of publication.

- All original code has been deposited in a repository (GitHub: https://github.com/minamimoto-lab/2021-Mimura-MarmoDREADD) and is publicly available as of the date of publication.
- Any additional information required to reanalyze the data reported in this paper is available from the lead contact upon request.

EXPERIMENTAL MODEL AND SUBJECT DETAILS

Animals

In total, eight laboratory-bred common marmosets were used. Four marmosets (Marmo1-4; 2 female/2 male; 2.5–4.0 years old; weight, 300–400 g; Table 1) were used for the chemogenetic manipulation study, and the remaining four animals (male; 1.5–5 years old, 300–330 g) were used for pharmacokinetics analyses (N = 4) and behavioral studies as non-DREADD controls (N = 2, Marmo5 and 6). Every cage was exposed to a 12-h/12-h light–dark cycle. Room temperature and humidity were maintained at 27–30°C and 40–50%, respectively. All experimental procedures were performed in accordance with the Guide for the Care and Use of Laboratory Animals (National Research Council of the US National Academy of Science) and were approved by the Animal Ethics Committee of the National Institutes for Quantum and of Radiological Sciences and Technology (#11-1038).

METHOD DETAILS

Viral vector production

AAV vectors (AAV2.1-hSyn1-hM3Dq-IRES-AcGFP, AAV2.1-TH-FLAG-hM3Dq, AAV2-CMV-hM3Dq, AAV2-CMV-AcGFP, AAV2-CMV-mKO, and AAV2.1-TH-AcGFP) were produced using a helper-free triple transfection procedure and purified via affinity chromatography (GE Healthcare, Chicago, USA). For production of AAV2.1 vector, the pAAV-RC1 plasmid-coding AAV1 capsid protein and the pAAV-RC2 plasmid-coding AAV2 capsid protein were transfected with the ratio of 1:9 (Kimura et al., 2021).

Surgery and vector injection

Surgeries were performed under aseptic conditions. We monitored body temperature, heart rate, and SpO2 throughout all surgical procedures. The marmosets were immobilized with ketamine and xylazine (25 and 2 mg/kg, intramuscularly) and then maintained under anesthesia using isoflurane (1–3%) during viral vector injection surgery. Prior to surgery, MRI and CT were performed to create overlay images to estimate the stereotaxic coordinates of target brain structures. According to the estimate, we opened burr holes (approximately 2 mm in diameter) on the skull for the injection needle. Viruses were pressure-injected using a 10-μL Nanofil Syringe (NANOFIL, WPI, Sarasota, USA) with a 33-gauge beveled Nanofil needle (NF33BV-2, WPI). The syringe was mounted into a motorized microinjector (UMP3T-2, WPI) that was held by a manipulator (model 1460, David Kopf) on the stereotaxic frame. We obtained CT scans and fused them with prescanned MR images during surgery to verify the location of the injection needle before and after insertion (Figure 1B). The injection needle was inserted into the brain, slowly moved down 1 mm beyond the target, and then kept stationary for 5 min, after which it was pulled up to the target location. The injection speed was set at 0.1 μL/min. After each injection, the needle remained *in situ* for 15 min to minimize backflow along the needle. Marmo1 and Marmo2 received an injection of an AAV vector carrying the hM3Dq and Aequorea coerulescens GFP constructs (AAV2.1-hSyn1-hM3Dq-IRES-AcGFP; 1.0 μL; 2.0×10^{13} particles/mL) on one side of SN and another injection of an AAV vector carrying the mKO gene (AAV2-CMV-mKO; 1.0 μL; 1.7×10^{13} particles/mL) into the other side. Marmo3 underwent a co-injection of AAV vectors (total, 2.0 μL) carrying the hM3Dq construct (AAV2-CMV-hM3Dq; 1.2×10^{13} particles/mL) and the AcGFP gene (AAV2-CMV-AcGFP; 0.3×10^{13} particles/mL) into one side of SN and an injection of an AAV vector carrying the mKO gene (AAV2-CMV-mKO; 2.0 μL; 1.7×10^{13} particles/mL) into the other side. Marmo4 was injected with two types of AAV vectors driven by a TH promoter, one expressing the hM3Dq fused with FLAG constructs (AAV2.1-TH-FLAG-hM3Dq; 0.5 μL; 2.5×10^{13} particles/mL) into one side of SN and the other expressing AcGFP (AAV2.1-TH-AcGFP; 0.5 μL; 1.7×10^{14} particles/mL) into the other side.

Drug administration

DCZ (HY-42110, MedChemExpress, NJ, USA) and CNO (Toronto Research, North York, Canada) were dissolved in 2.5% dimethyl sulfoxide (DMSO, FUJIFILM Wako Pure Chemical., Osaka, Japan). These stock solutions were diluted in saline to a final volume of 0.1 mL for subsequent experimentation. For behavioral testing,

DCZ was administered via IP (3 μg/kg) or PO (10 μg/kg). For pharmacokinetic studies, DCZ solution (100 μg/kg) was administered via IP or PO. For PET, DCZ (3 μg/kg) or CNO solution (10 mg/kg) was injected intravenously.

PET

PET was performed using a microPET Focus 220 scanner (Siemens Medical Solutions, PA, USA). The marmosets were maintained under anesthesia using isoflurane (1–3%) during all PET procedures. A transmission scan using a spiraling ^{68}Ge point source was performed to correct attenuation before a bolus injection of the radioligands [^{11}C]DCZ or [^{18}F]FDG. Emission scans were acquired in 3D list mode with an energy window of 350–750 keV after an IV bolus injection of [^{11}C]DCZ (97.3–105.9 MBq) or [^{18}F]FDG (68.1-78.1 MBq). For PET scans using [^{18}F]FDG, each animal received IV treatment with DREADD agonists (10 mg/kg CNO or 3 μg/kg DCZ) or vehicle (DMOS) in advance to permit peak chemogenetic activation via hM3Dq (30 min for CNO or 1 min for DCZ treatment).

Histology

Marmosets were sedated with 25 mg/kg ketamine hydrochloride administered intramuscularly and then euthanized using an overdose of 100 mg/kg sodium pentobarbital (Somnopentyl, BCM International, Hillsborough, USA) administered intraperitoneally. Next, they were intracardially perfused with 0.1 M potassium phosphate-buffered saline (PBS), followed by 4% paraformaldehyde (Merck, Whitehouse Station, USA) in 0.1 M PBS. The brains were removed from the skull, postfixed in the same fresh fixative overnight, and saturated with 30% sucrose in PB at 4°C. A freezing microtome was used to cut coronal sections serially at a thickness of 40 μm. Every 12th section was mounted onto gelatin-coated glass slides and Nissl-stained with 1% cresyl violet.

For immunoperoxidase staining, the sections were incubated for 2 days at 4°C with rabbit anti-GFP antibody (1:2,000; Thermo Fisher Scientific, Waltham, USA). The sections were then incubated with biotinylated donkey anti-rabbit IgG antibody (1:1,000; Jackson Laboratories, Farmington, USA), followed by treatment with an avidin-biotin-peroxidase complex kit (ABC Elite; 1:100; Vector Laboratories, Burlingame, USA). To visualize the antigen, the sections were reacted for 10–20 min in 0.05 M Tris-HCl buffer (pH 7.6) containing 0.04% diaminobenzene tetrahydrochloride (FUJIFILM Wako Pure Chemical, Osaka, Japan), 0.04% $NiCl_2$, and 0.002% H_2O_2. The reaction time was adjusted to make the density of background immunostaining almost identical throughout the cases. These sections were counterstained with 0.5% neutral red, mounted onto gelatin-coated glass slides, dehydrated, and coverslipped.

Behavioral testing

Behavioral experiments were conducted in a sound-attenuated room (O'hara & Co., Ltd., Tokyo, Japan; 2.4 (h) × 1.2 (w) × 1.6 (d) m^3), which was apart from the colony room. Any vocalization sounds from the colony room could not be detected in that room. Temperature was maintained at 27–31°C and relative humidity was 30–40%. The internal space of the sound-attenuated room was ventilated and illuminated with fluorescent lighting. The experiments were performed between 11:00 and 16:00. Before the experimental sessions, each subject was transferred individually from the colony room to the experimental room in a small transport chamber (165 (h) × 140 (w) × 255 (d) mm^3, Natsume Seisakusho, Tokyo, Japan) and placed in a transparent acrylic cylinder chamber (radius 0.5 m × height 0.5 m) in the sound-attenuated room (Video S3). The subjects were allowed to adapt to the transport procedure and experimental environment for 4 consecutive days prior to behavioral testing. For 3D data acquisition, the test chamber was placed on a foothold with a green floor (1 m height), and four depth cameras (RealSense Depth Camera D435, Intel, Santa Clara, USA) were placed around the chamber at the 3, 6, 9, and 12 o'clock positions. The cameras were connected in parallel to a PC (Windows 10, 64-bit) using USB-C cables (U3S1A01C12-050, Newnex Tech., Santa Clara, USA; distance was 1–5 m).

The behavioral experiment started when a marmoset was put in the chamber, and the recording of the movements lasted up to 90 min (Figure 4E). The subject was returned to the colony room after the end of the recording session. The experiments were performed once a day for each subject.

Marmo1 and 2 were examined under three conditions (vehicle treatment, DCZ treatment, and 24 h after DCZ treatment, Figure 4E) using a repeated-measures design with a total of four repetitions of either PO or IP administration. In the PO condition, animals were fed a piece of sponge cake (approximately 2 g) containing DCZ solution (10 μg/kg) or vehicle (DMSO) on the floor of the test chamber at the start of the session (Video S1). In the IP condition, the marmosets were injected with either DCZ solution (3 μg/kg) or vehicle

immediately before the experiment began. Note that the behavioral tests in the IP and PO conditions were performed with an interval of approximately one year, the latter time point being when pharmacokinetic studies were conducted to find the optimal DCZ dosage for the PO condition. Marmo4 was examined under vehicle and DCZ-PO conditions with two repetitions.

Markerless 3D MTS

A novel markerless 3D MTS was developed to track and analyze the behavior of freely moving marmosets based on our previous systems designed for rats (Matsumoto et al., 2013, 2014) and macaque monkeys (Nakamura et al., 2016) by adding a hue filter to properly extract the point cloud of the marmoset and optimizing the parameters of the skeletal model to track their body parts (Figure 4B). Our MTS software package for depth camera calibration, 3D data acquisition, and fundamental setup for physical simulation are available online (3DTracker-FAB, 3dtracker.org), and this software allowed us to robustly estimate the 3D trajectory of marmoset body parts semi-automatically as follows. First, the entire surface of a marmoset body was digitized as a 3D point cloud (Figure 4A) based on depth images captured from the four depth cameras using the functions of Intel Realsense SDK (github.com/IntelRealSense/librealsense) and the Point Cloud library (pointclouds.org). Then, in the first frame of the video, a marmoset skeleton model was manually located near the 3D point cloud and automatically fitted by the physics-based algorithm. The skeleton model consisted of four spheres representing each body part (*Head*, *Neck*, *Body*, and *Hip*) and connected with joints rotating with different ranges corresponding to the anatomical constraints (Figure 4B, see Video S2). The fitting algorithm works as if it physically houses the skeleton model into the 3D point cloud of the marmoset with the aid of the Bullet Physics Library (ver. 2.8.1, bulletphysics.org). In the simulation, the three types of forces from the 3D points to the skeleton spheres were assumed to stabilize the model within the 3D point cloud, namely, attraction forces, repulsive forces, and the attraction force from the Hip sphere toward the floor (Matsumoto et al., 2013, 2014). Finally, the resultant positions of the body skeleton spheres were recorded and used as the initial position for the next frame. The average error between the estimated *Head* positions projected onto 2D images and their 'ground-truth' based on manual tracking were 0.26 $\pm$ 0.04 and -0.41 $\pm$ 0.05 cm, on the X- and Y-axes, respectively, (mean $\pm$ sem, Figure S3).

MRI and CT

MRI and X-ray CT were performed under general anesthesia in the same manner as PET. MR T2-weighted images were obtained on a 7-tesla, 200-mm-bore MRI (BioSpec AVANCE-III, Bruker, BioSpin, Rheinstetten, Germany) with a volume resonator with an 85-mm inner diameter for transmission (Bruker, BioSpin) and an 8-channel phased array coil for reception (RAPID Biomedical, Rimpar, Germany). The obtained data were reconstructed using ParaVision 5.1 (Bruker BioSpin). We used a 3D rapid acquisition enhancement sequence according to the following parameters: repetition time = 2500 ms; echo time = 8.93 ms; field of view (FOV) = 26 × 35 × 25.6 mm^3, and matrix size = 128 × 128 × 64. CT scans were obtained using a cone-beam CT system (Accuitomo170, J. Morita Co., Kyoto, Japan), which was operated under the following conditions: tube voltage = 90 kVp, tube current = 5 mA, exposure time = 17.5 s, FOV = 140 (diameter) × 100 (height) mm, voxel size = 0.25 × 0.25 × 0.5 mm^3, and gray intensity of 16 bits. Overlay MR and CT images were created using PMOD image analysis software ver. 3.7 (PMOD Technology Ltd., Switzerland).

Pharmacokinetics analysis

Acute blood samples were collected from a saphenous vein using a 24-gauge indwelling needle (SR-OT2419C, Terumo Co., Tokyo, Japan) from four conscious marmosets immobilized on a retention holder (CL-4532, CLEA Japan Inc., Japan). Samples were collected at 15, 30, 60, 90, and 120 min and 24 h after IP or PO DCZ treatment (100 μg/kg). Plasma was separated, and samples (50 μL) were diluted in 150 μL of methanol and stored at −80°C until analysis. Samples were dissolved in 50 μL of 50% methanol followed by 20 μL of Granisetron solution (10 ng/mL, internal standard). Quantification of DCZ and its major metabolites DCZ-N-oxide and C21 was performed using a Shimadzu UHPLC LC-30AD system (Shimadzu) coupled to a tandem MS AB Sciex Qtrap 6500 system (AB Sciex).

QUANTIFICATION AND STATISTICAL ANALYSIS

PET data analysis

PET data analyses were performed using PMOD image analysis software to estimate stereotaxic coordinates of the target brain structure. The standardized radioligand uptake value was calculated as regional

radioactivity (Bq/cm^3) × body weight (g)/injected radioactivity (Bq) at 30–90 min post injection. BP_{ND} was estimated using a parametric multilinear reference tissue model (MRTMo) with the cerebellum as reference region (Nagai et al., 2020; Ichise and Ballinger, 1996). The values were compared using statistical methods with R version 3.6.1 and the formula $BP_{ND} \sim side + individuals$ (pairwise *t*-test, df = [1, 2, 2], Figure 1D), where *side* is the side ipsilateral or contralateral to the hM3Dq vector-injected side of SN. For [^{18}F]FDG-PET analysis, standardized uptake values (SUVR) were calculated at 30-90 min post injection using whole brain uptake as reference. Parametric images for an increase in the SUVR (ΔSUVR, Figure 2A) was constructed by subtraction of the mean SUVR images of vehicle from agonist (DCZ or CNO) administration.

Behavioral data analysis

Behavior data analyses were performed using R version 3.6.1 and its package tidyverse version 1.3.0 (Wickham et al., 2019). The trajectory of body parts was filtered with a loess filter using the stats::loess() function with span = 1/300 and downsampled to 10 frames/s (Figure 5A). The spatial head movement speed was calculated frame-by-frame and divided into horizontal and vertical vectors (Figures 4C and 5B). The body axis was defined as the vector from the *Body* center to the *Head center*, and θ_{rot} was calculated from its horizontal component with a positive value for the contralateral direction to the activated side (Figure 4D). To quantify the biased rotation behavior, the number of total contraversive rotations was calculated from the cumulative sums of θ_{rot} as follows:

$$\Delta\theta = \sum_{t=t_0}^{t_1} \theta_{rot} \qquad \text{(Equation 1)}$$

The number of contraversive rotations in 5 min (Figure 5E) was defined as $\Delta\theta_1/2\pi$, where $\Delta\theta_1$ was the cumulative sum in the time window $[t_0,\ t_1]$ as follows:

$$t_0 \in \{0,\ 5, \ldots, 85_{min}\},\ t_0 \le t_1 \le t_0 + 5_{min}. \qquad \text{(Equation 2)}$$

The number of contraversive rotations in 10 min (Figures 5E and 5F) was defined as $\Delta\theta_2/2\pi$, where $\Delta\theta_2$ was the cumulative sum in the sliding time window $[t_0,\ t_1]$ as follows:

$$t_0 \in [0,\ 80_{min}],\ t_0 \le t_1 \le t_0 + 10_{min}. \qquad \text{(Equation 3)}$$

To quantify the effects of DCZ treatment, the deviation score R_{in} was calculated from $\Delta\theta_2$ as the ratio of staying time under the 95% confidence interval of in the vehicle condition (Figure 5G) as follows:

$$R_{in} = \frac{T\left[\Delta\theta_2 \in 95\%CI_{vehicle\ \Delta\theta_2}\right]}{T_{test\ \ duration}}. \qquad \text{(Equation 4)}$$

These parameters were compared between the treatment conditions across individuals as value ∼ individuals + treatment for two-way ANOVA and Tukey's honestly significant difference test.